Scilight

Photocatalysis

https://www.sciltp.com/journals/photocatalysis

Article

Photocatalytic Oxidation of Cyclohexane in a Biphasic System Using Rapidly Synthesized Polymeric Carbon Nitride Films

Ayelet Tashakory, Venugopala Rao Battula * and Menny Shalom *

Department of Chemistry and Ilse Katz Institute for Nanoscale Science and Technology, Ben-Gurion University of the Negev, Beer-Sheva 8410501, Israel

* Correspondence: battula@bgu.ac.il (V.R.B.); mennysh@bgu.ac.il (M.S.)

How To Cite: Tashakory, A.; Battula, V.R.; Shalom, M. Photocatalytic Oxidation of Cyclohexane in a Biphasic System Using Rapidly Synthesized Polymeric Carbon Nitride Films. *Photocatalysis* **2025**, *1*(1), 4. https://doi.org/10.53941/photocatalysis.2025.100004

Received: 11 September 2025
Revised: 2 November 2025
Accepted: 5 November 2025
Published: 12 November 2025

Abstract: The oxidation of cyclohexane (CHA) to cyclohexanol and cyclohexanone (collectively known as KA oil) is a key C–H activation reaction and holds a central step in Nylon™ production. However, traditional processes suffer from low conversion and complex reaction conditions. Photocatalytic approaches under ambient conditions offer a sustainable alternative, though most rely on suspended powders with challenges in light management, catalyst recovery, and scalability. Here, we demonstrate the use of immobilized carbon nitride films for visible light-driven oxidation of CHA in a biphasic CHA–water system at a mild temperature. The system achieves high KA oil yields without stirring, enabling better light utilization and operational simplicity. Product selectivity proved to depend on the type of acid added: HCl favors cyclohexanone, while HBr enhances cyclohexanol formation. Mixtures of both acids allow fine-tuning of the product ratio. These findings highlight the potential of scalable CN-based photocatalyst panels for energy-efficient KA oil production under benign conditions. The highest product yield was achieved after 6 days in a biphasic CHA + 1 M HCl system, obtaining 155 μM cm^{-2} KA oil.

Keywords: carbon nitride; photocatalysis; cyclohexane oxidation; KA oil; C–H activation

1. Introduction

The partial oxidation of cyclohexane (CHA) by molecular oxygen (O_2) yields a mixture of cyclohexanone and cyclohexanol, commonly known as KA oil—a feedstock chemical with an annual production of 8000 tons, mainly used for the manufacture of Nylon™ [1,2]. The current industrial process for KA oil production, which involves a gas phase CHA oxidation by O_2, requires high temperature/pressure and suffers from low CHA conversion (4–15%) and partial heat recovery [1–4]. Achieving liquid phase CHA oxidation at room temperature/ambient pressure could simplify the overall KA oil production process by eliminating the high energy requirements, and also reducing the potential for greenhouse gas emissions.

Recently, visible light-driven heterogeneous photocatalysis has emerged as a tool for various fundamental organic reactions [5–7]. Compared to conventional thermal catalysts, photocatalysts can readily generate highly reactive oxygen species (ROS), such as singlet oxygen, superoxide radicals, and hydroxyl radicals, enabling several thermodynamically uphill reactions, including CHA oxidation under environmentally benign conditions [2,5]. Over the years, a variety of photocatalysts or photocatalytic systems, typically involving a photocatalyst powder stirred in pure CHA or a solvent containing CHA under light illumination, have been proposed for selective CHA oxidation to KA oil [8–15]. Despite this progress, photocatalytic CHA oxidation to KA oil remains far from economically viable for direct scale-up, due to low KA oil yield and intrinsic limitations of powdered photocatalytic systems, such as

sedimentation, poor light management, and difficult catalyst recovery. Thus, developing efficient photocatalyst panels, consisting of a thin layer of photocatalyst coated on a substrate, for CHA oxidation in practically scalable batch or flow configurations is highly appealing for sustainable Nylon™ production.

Polymeric carbon nitride (CN) is a metal-free, low-cost semiconductor that has emerged as a sustainable photocatalyst, with pioneering studies establishing its structural framework and visible-light activity [16–21]. Its tunable band gap (~2.7 eV), chemical stability, and ability to generate reactive radical species have made it a promising platform for selective organic reactions, including photocatalytic C–H activation and oxidation [17,22–27].

In this study, we demonstrate the advantage of CN panels for high-yield photooxidation of CHA to KA oil in a biphasic CHA-water system at elevated temperatures (Scheme 1). We use CN as the photocatalyst due to its tunable band positions for ROS generation, high stability, and simple synthesis routes. We observed that the addition of HCl dramatically improves the cyclohexanone yield, while replacing it with HBr surprisingly shifts the product distribution toward cyclohexanol. Furthermore, a scale-up reaction was demonstrated by a 6 × 2 cm^2 CN panel over 6 days, yielding cyclohexanone and KA oil at average rates of 26.4 and 10.8 mM m^{-2} h^{-1}, respectively.

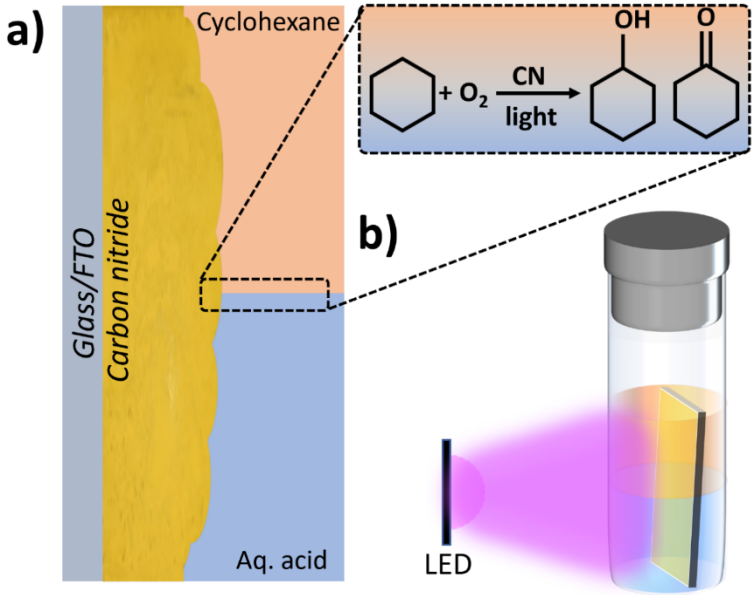

Scheme 1. An illustration of (**a**) the CN panels used as the catalyst in a biphasic CHA-water system, which drastically improves product yield; and (**b**) the photocatalytic oxidation reaction setup.

2. Results and Discussion

The carbon nitride (CN) films used in the photocatalytic experiments were synthesized following a procedure similar to that described in our previous study [28], as detailed in the Experimental Section. In this work, we focused on four CN films previously reported in the abovementioned work, all synthesized using a 3:1 melem-to-melamine supramolecular assembly and calcined at 680 °C. The samples differ in calcination time (10 or 20 min) and in the presence or absence of additional melem powder within the "sandwich" configuration. These are designated as CN-10, CN-M10, CN-20, and CN-M20, where the number indicates the calcination duration and the "M" denotes the presence of melem powder. Among these, CN-10 exhibited the highest photocatalytic activity, as will be discussed later. Therefore, this film was selected for comprehensive characterization and photocatalytic measurements. A detailed comparison of its properties with those of other films is provided in Supplementary Materials Figure S1. Although CN-10 exhibits the highest photocatalytic activity, comparative characterizations, including structural analyses such as X-ray diffraction (XRD) and Fourier-transform infrared (FTIR) spectroscopy, as well as optical measurements such as photoluminescence (PL), UV-Vis diffuse reflectance spectra, and Tauc plot analysis, do not reveal obvious advantages that could directly account for its higher performance.

The XRD pattern of CN-10 exhibits two characteristic peaks of carbon nitride: an in-plane (100) reflection at 13.3°, and a broad (002) interlayer stacking peak at 27.3° [29], indicative of an amorphous structure (Figure 1a). The FTIR spectrum of CN-10 shows vibrational bands in the range of 1100–1700 cm^{-1}, corresponding to C=N stretching modes of heterocyclic units. A sharp peak at ~800 cm^{-1} is assigned to the breathing vibrations of heptazine rings, while a broad signal around 3200 cm^{-1} is attributed to N–H stretching vibrations, arising from incomplete polymerization (Supplementary Materials Figure S2) [28]. X-ray photoelectron spectroscopy (XPS)

data are presented in Supplementary Materials Figure S3. The C 1s spectrum of CN-10 can be deconvoluted into four distinct peaks corresponding to C=C, C–NH_2, N=C–N, and C=O, located at 284.8 eV, 286.3 eV, 288.0 eV, and 288.8 eV, respectively [30,31]. The C=C signal arises from the carbon-rich environment, while the C=O is attributed to surface oxidation occurring during synthesis. This oxidation is likely due to residual oxygen present in the furnace, as the outlet side remains open during the thermal polymerization process. The N 1s spectrum can similarly be deconvoluted into four peaks attributed to pyridinic N, N–H_2, N–H, and quaternary N, located at 398.5 eV, 399.0 eV, 400.1 eV, and 401.1 eV, respectively [32,33]. The XPS survey spectrum presented in Supplementary Materials Figure S3c verifies that no aluminium contamination occurred during the fast heating process. Elemental composition analysis based on XPS reveals atomic percentages of 39.39% carbon, 57.02% nitrogen, and 3.59% oxygen (Supplementary Materials Table S1). The UV–vis diffuse reflectance spectrum (Supplementary Materials Figure S4) was used to determine the optical bandgap via Tauc plot analysis, revealing a bandgap energy of 2.82 eV (Figure 1b). PL spectroscopy, performed with an excitation wavelength of 380 nm, showed a strong emission peak centered at 460 nm (Supplementary Materials Figure S5).

Top-view scanning electron microscopy (SEM) images (Figure 1c) show a heterogeneous morphology characterized by round, cage-like structures. These features contribute to an increased surface area, thereby enhancing the photocatalytic performance. The use of a rapid-heating synthesis method likely contributes to this diverse morphology due to non-uniform polymerization. Cross-sectional SEM imaging confirms a uniform film thickness of approximately 20 µm, with the morphological features also visible in the cross-sections (Figure 1d). Additional SEM images at varying magnifications are provided in Supplementary Materials Figure S6.

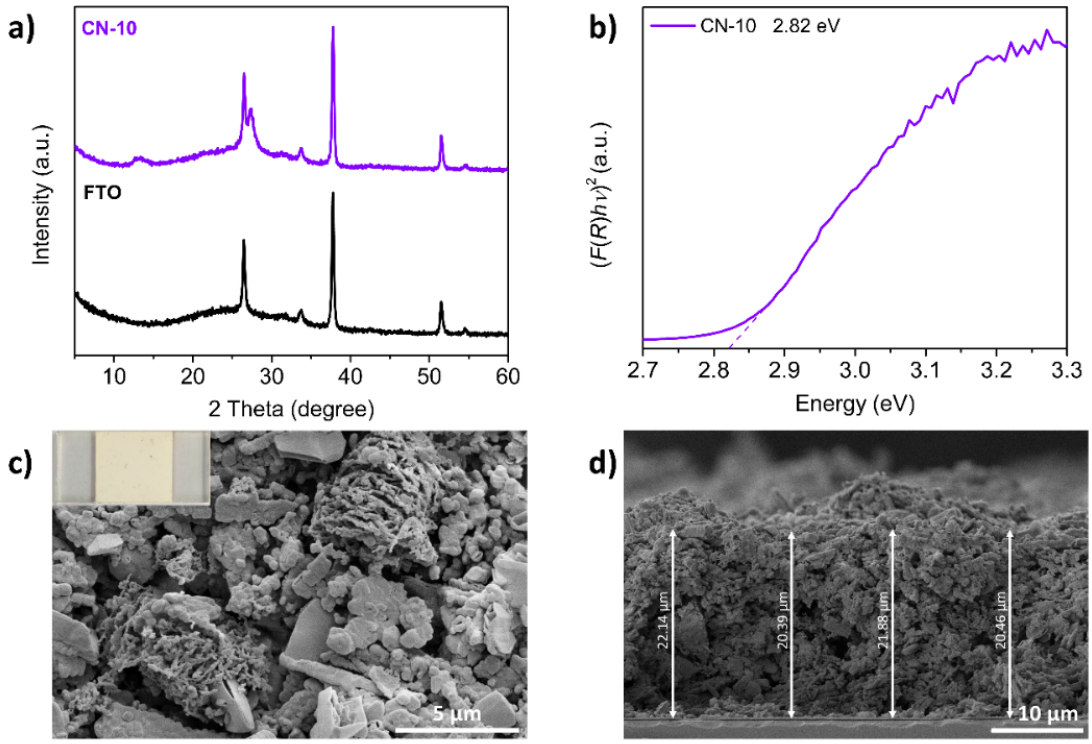

Figure 1. (**a**) XRD pattern of CN-10; (**b**) Tauc plot analysis for the determination of the optical bandgap of CN-10; (**c**) Top-view (inset: digital picture of CN-10); and (**d**) cross-sectional SEM images of CN-10.

3. Photocatalytic Cyclohexane Oxidation Measurements

The photocatalytic cyclohexane oxidation performance of the as-synthesized CN films (CN-10, CN-M10, CN-20, and CN-M20) was first evaluated in a multi-photoreactor under 390 nm LED illumination for 24 h at 25 °C (Supplementary Materials Figure S7). Prior to each measurement, the reaction solution (5 mL) was purged with O_2 for 20 min, followed by an additional 20-min O_2 purge of the sealed reactor headspace. Among all CN panels, the CN-10 exhibited the highest activity, yielding 240 µM cm^{-2} of cyclohexanol, 180 µM cm^{-2} of cyclohexanone, and 210 µM cm^{-2} of KA oil (cyclohexanol + cyclohexanone). Consequently, CN-10 was selected for further investigation (Supplementary Materials Figure S8a). Further, CN-10 films were also deposited on two other surfaces: a microscope glass slide and the glass (non-conductive) side of FTO, and their activity was compared

with that of FTO (Supplementary Materials Figure S8b). FTO exhibited improved activity, which may be ascribed to its higher surface roughness; therefore, we used CN-10 prepared on FTO.

To find the optimal reaction conditions, we investigated the effect of reaction temperature. As shown in Figure 2a, the best performance was achieved at 35 °C, yielding 260 μM cm^{-2} of cyclohexanol, 565 μM cm^{-2} of cyclohexanone, and 410 μM cm^{-2} of KA oil. These results suggest that the elevated temperature not only improved overall yield but also favours the more oxidized product, cyclohexanone.

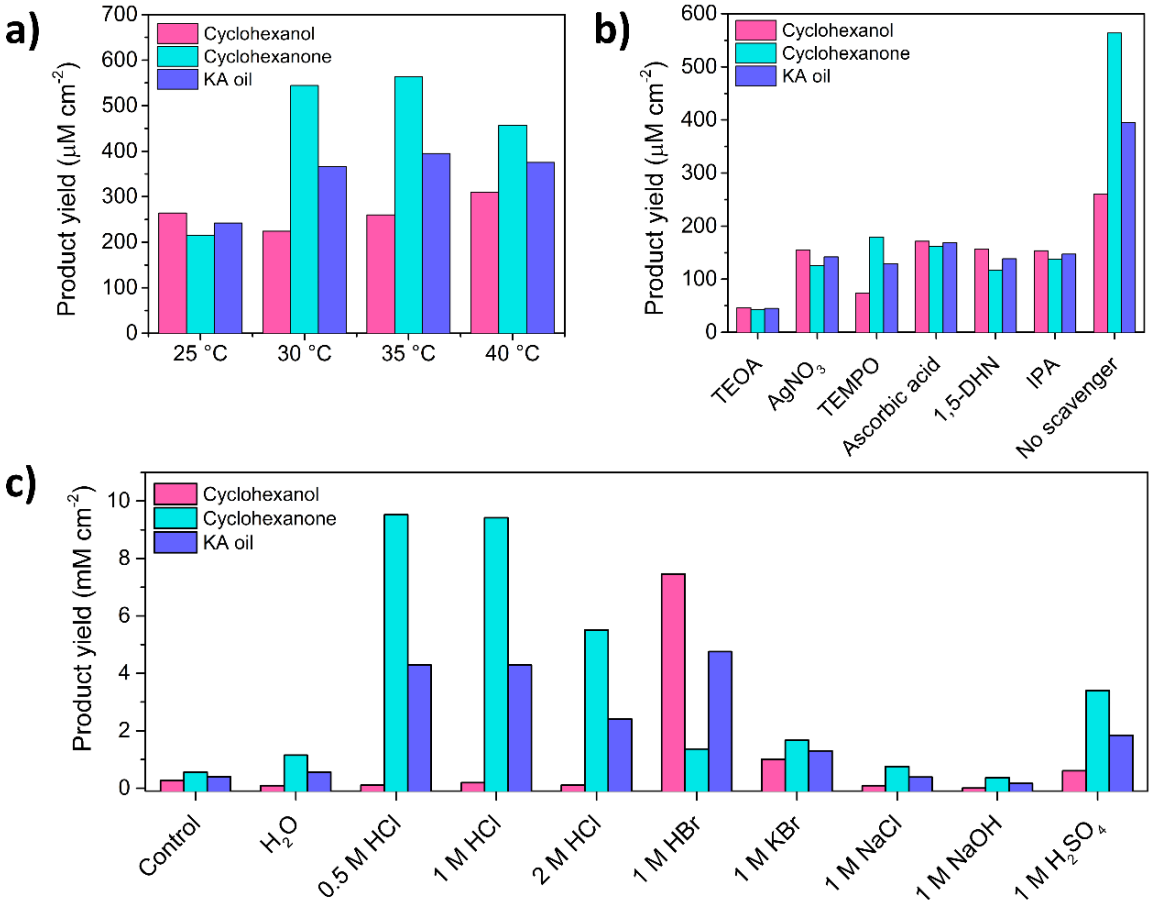

Figure 2. Photocatalytic oxidation of cyclohexane measurements. (**a**) Temperature optimization; (**b**) Trapping agents experiments using 10 mM of various scavengers in CHA: TEOA, $AgNO_3$, TEMPO, ascorbic acid, 1,5-dihydroxynaphthalene (1,5-DHN), and isopropanol (IPA); (**c**) Photocatalytic activity of CHA in a biphasic system, compared to the control reaction with pure CHA. Systems include CHA combined with: H_2O, 0.5 M HCl, 1 M HCl, 2 M HCl, 1 M HBr, 1 M KBr, 1 M NaCl, 1 M NaOH, and 1 M H_2SO_4.

3.1. Mechanistic Investigation

The photocatalytic CHA oxidation was previously discussed in the literature [2,10,34]. According to these reports, primarily the photogenerated holes and electrons, as well as ROS, participate in the CHA oxidation to KA-oil. However, to gain further insight into the photocatalytic mechanism under our experimental conditions, a series of scavenger experiments was conducted using 10 mM of various trapping agents in cyclohexane (CHA): TEOA for holes, $AgNO_3$ for electrons, TEMPO for radicals, ascorbic acid for superoxide radicals, 1,5-dihydroxynaphthalene (1,5-DHN) for singlet oxygen, and isopropanol (IPA) for hydroxyl radicals. As shown in Figure 2b, all scavengers led to a decrease in product yield, with the most significant reduction observed in the presence of TEOA, highlighting the crucial role of photogenerated holes in the reaction. The other scavengers showed comparable effects, suggesting multiple ROS are involved. Based on these observations and previous studies [35], a plausible mechanism for the photocatalytic CHA oxidation is illustrated in Scheme 2. Upon photoexcitation, CN promotes CHA oxidation through two pathways: electron transfer and energy transfer. In the former, excited CN reduces molecular oxygen (O_2) to superoxide radicals ($O_2^{\bullet-}$), which drive the formation of cyclohexanol and cyclohexanone. In the latter, energy transfer generates singlet oxygen ($^1O_2$), which directly oxidizes CHA to the same products.

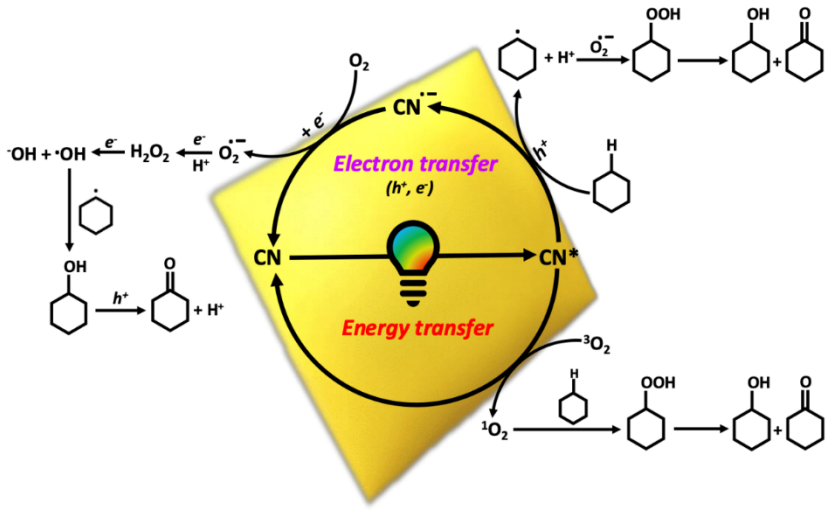

Scheme 2. Proposed mechanism of CHA photooxidation over CN via electron transfer (superoxide formation) and energy transfer (singlet oxygen formation), both giving cyclohexanol and cyclohexanone.

3.2. Effect of Aqueous Phase Addition

To further enhance the efficiency and selectivity of CHA oxidation, hydrochloric acid (HCl) was chosen as an additive according to previous reports [9,10,36–39]. Addition of aq. HCl to our batch system creates a biphasic reaction system. Since CN films are immobilized and unlike powders, do not suffer from sedimentation over time, the system was designed to ensure the liquid–liquid interface remained in contact with the CN-10 film (Supplementary Materials Figure S9). Moreover, this biphasic system enables in situ separation and replacement of the CHA phase without an additional catalyst recovery step. Various aqueous phases were tested: DI water, 0.5 M HCl, 1 M HCl, and 2 M HCl. All acidified systems exhibited significantly increased product yields compared to pure CHA, with 0.5 M and 1 M HCl producing the highest yields (~9.5 mM cm^{-2} cyclohexanone and ~4.3 mM cm^{-2} KA oil). Since 1 M HCl also gave slightly higher cyclohexanol yield (0.18 mM cm^{-2} vs. 0.12 mM cm^{-2} for 0.5 M HCl), it was selected as the optimal condition (Figure 2c). To verify the reproducibility of the photocatalytic performance, the reaction with 1 M HCl was repeated three times under identical experimental conditions [40]. The product yields obtained in all runs showed negligible variation, confirming the reliability and consistency of the photocatalytic results (Supplementary Materials Figure S10).

To understand the origin of the significant yield enhancement, we conducted additional experiments using various halide acids and salts beyond 1 M HCl, including 1 M HBr, 1 M KBr, and 1 M NaCl. Minor improvements were observed with KBr and NaCl, however 1 M HBr drastically increased cyclohexanol yield (7.4 mM cm^{-2}), while 1 M HCl remained more effective for cyclohexanone production. Based on the well-established mechanism of HCl-assisted cyclohexane oxidation reactions, we propose the following reaction pathway for our system: Upon illumination, the CN generates electron-hole pairs. Halide ions (Cl^- or Br^-) in the aqueous phase can be oxidized by the photogenerated holes to produce halogen radicals ($Cl^\bullet$ or $Br^\bullet$, respectively). These radicals, together with hydroxyl radicals, act as efficient hydrogen atom abstractors, removing hydrogen from cyclohexane to form cyclohexyl radicals. The resulting radicals subsequently react with reactive oxygen species (ROS) to yield the oxidized products, cyclohexanone and cyclohexanol [37,38,41]. To the best of our knowledge, no previous reports have described HBr-assisted cyclohexane oxidation using CN as a catalyst. We therefore suggest that the observed difference in product selectivity originates from the distinct oxidation strengths of the halogen radicals. Given the lower bond dissociation energy of H-Br compared to H-Cl, $Br^\bullet$ acts as a milder oxidant than $Cl^\bullet$, thereby favouring alcohol formation over further oxidation to the ketone [42–44].

To determine whether the product yield enhancement originates from the pH of the solution or the presence of halide ions, we also tested 1 M NaOH and 1 M H_2SO_4. Under basic conditions, the product yield was even lower than in the control experiment. When the sulfuric acid was used for the aqueous phase, the product yield was higher than in the control experiment, but lower than the halide acids. These results confirm that both factors contribute to the observed yield improvement through a synergetic effect, with the acidic environment serving as the primary factor (Figure 2c). Interestingly, when mixtures were prepared by combining equal volumes of 1 M or 2 M HCl and 1 M or 2 M HBr solutions, resulting in effective concentrations of 0.5 M or 1 M for each acid, the yield of cyclohexanol was intermediate between those obtained with HCl or HBr individually and increased proportionally with the effective concentration of HBr. In contrast, the yield of cyclohexanone was even lower

than that obtained with HBr alone and remained unchanged between the two tested mixture concentrations (Supplementary Materials Figure S11). These findings suggest the potential to tune the product distribution of CHA oxidation reactions by modifying the nature and combination additives. It is important to mention that the reactions with HCl and HBr also yield halide byproducts, such as chlorocyclohexane and bromocyclohexane. Since this study focuses on the production of KA oil, we did not quantify these products. GC chromatograms and MS spectra of the products obtained in the reactions with pure CHA, and the 1 M HCl and 1 M HBr biphasic systems can be found in the Appendix A.

Moreover, when Ar was purged instead of O_2, the product yield was significantly lower in pure CHA and in a biphasic system of CHA + 1 M HCl, confirming the essential role of oxygen in the reaction (Supplementary Materials Figure S12).

3.3. Advantages of CN Films Over CN Powders

Following yield optimization, we performed two key experiments to demonstrate the advantages of using CN films over powders. First, the CN-10 film was reused in three consecutive photocatalytic cycles with negligible difference in activity, confirming its good stability and recyclability (Figure 3a). In contrast, CN powders require post-reaction separation steps, during which some material is inevitably lost, limiting their reusability. Second, the performance of the CN-10 film was compared to CN powder under 1 M HCl conditions. Since the powder was obtained by scratching a CN-10 film of identical area to the one used in the film-based measurements, we assume that a comparable amount of catalyst was used in each reaction. Three conditions were tested: CN film without stirring, CN powder with stirring, and CN powder without stirring (Figure 3b). While stirring improved the performance of the powder due to constant mixing, the CN film still outperformed the unstirred powder. This highlights the benefit of using immobilized films in biphasic systems, as they maintain stable contact with both phases throughout the reaction without the need for mechanical mixing.

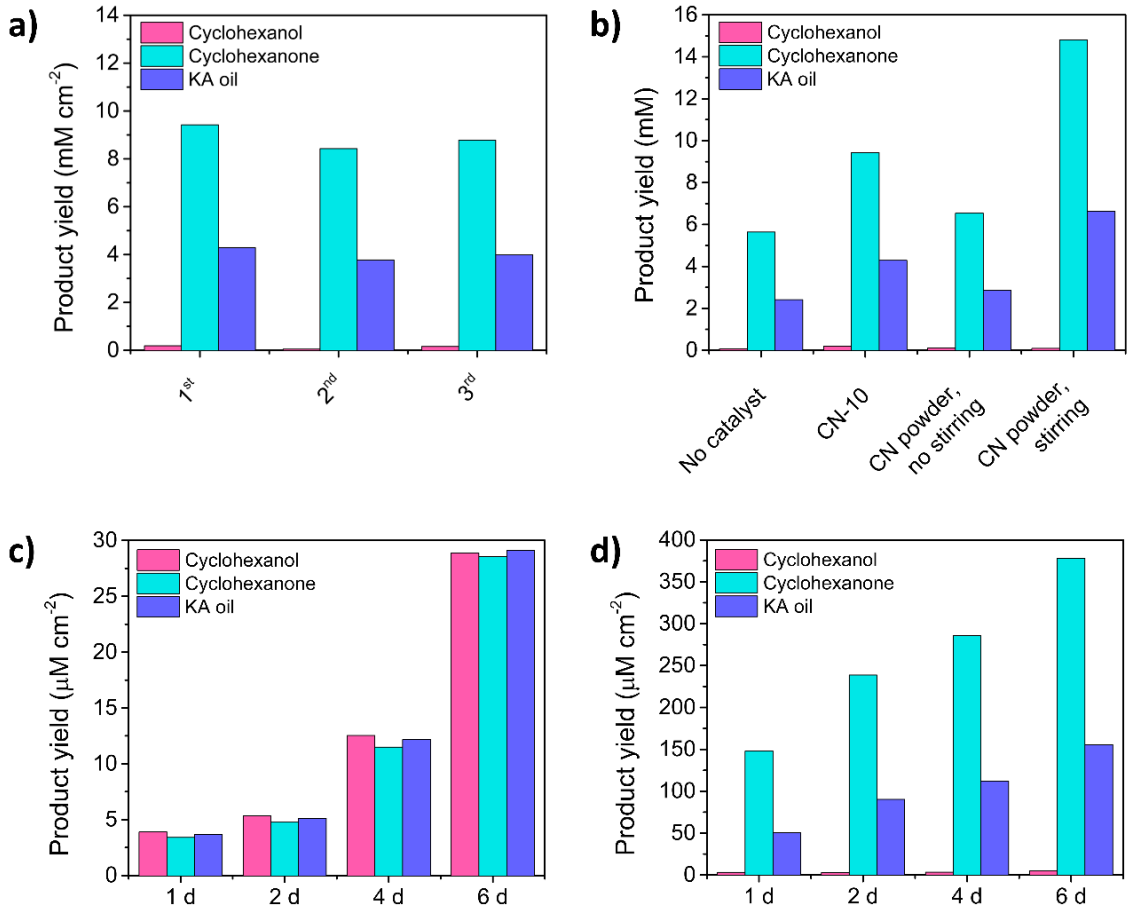

Figure 3. (**a**) Recyclability of CN-10, as demonstrated in three consecutive photocatalytic cycles with negligible difference in activity; (**b**) Comparison of the photocatalytic performance of CN-10 film, with CN-10 powder with and without stirring. Scale-up photocatalytic CHA oxidation using a 12 cm^2 CN-10 film, measured for 6 d; (**c**) in pure CHA; and (**d**) in a biphasic system of CHA + 1 M HCl.

3.4. Long-Term, Large-Scale Measurements

Finally, we demonstrate the scale-up experiments using 6 × 2 cm² CN-10 films in a 45 mL total solution volume, under white LED light illumination (100 W, λ > 400 nm; the irradiation spectrum is provided in Supplementary Materials Figure S13). Two systems were tested: pure CHA (45 mL) and biphasic CHA (35 mL) + 1 M HCl (10 mL). The reaction test tubes were purged with O_2 for 1 h before the start and every 24 h. Samples were collected after 1, 2, 4, and 6 days. In pure CHA, cyclohexanol and cyclohexanone yields remained comparable throughout, unlike the small-scale experiments (under 390 nm), where cyclohexanone was dominant, suggesting that white LED favours cyclohexanol production (Figure 3c). In the presence of 1 M HCl, cyclohexanone remained the major product, with yields 45–85 times higher than cyclohexanol, consistent with the small-scale results (Figure 3d). Product evolution over time in both systems is shown in the GC-MS curves in Supplementary Materials Figure S14. A comparison of the KA oil yield in the presence and in the absence of HCl vs. time is presented in Supplementary Materials Figure S15. Overall, the highest product yield under the abovementioned conditions, achieved after 6 days in the biphasic CHA + 1 M HCl system, is 5 μM cm^{-2} cyclohexanol, 378 μM cm^{-2} cyclohexanone, and 155 μM cm^{-2} KA oil.

3.5. Post-Reaction Film Characterization

The CN-10 film used in the large-scale reaction with 1 M HCl was characterized to assess changes induced by the reaction environment. The film was divided into two regions: the lower portion in contact with the aqueous phase and the upper portion exposed to the organic phase, and both were compared to the pristine CN-10 film. XRD and FTIR analyses revealed no significant structural changes, with spectra identical to those of the original film (Supplementary Materials Figure S16). Cross-sectional SEM images reveal deterioration in the film's adhesion to the FTO substrate in both the aqueous and organic phases when compared to the original CN-10 film, with more pronounced delamination observed in the organic phase, where the film separated into two layers. Despite this, no significant morphological differences are observed between the two parts of the used film, as confirmed by top-view SEM images (Supplementary Materials Figure S17). XPS data of the film before and after measurements exhibit a positive shift to higher binding energy in the sp^2 carbon-nitrogen bond in both the C 1s and N 1s spectra, suggesting that the HCl is not only physically absorbed, but also chemically interacts with the CN, causing protonation or surface structural modification (Supplementary Materials Figure S18). XPS composition analysis indicated an increased oxygen content compared to the pristine CN-10 film and the presence of less than 1 at.% chlorine in both sections of the used film, likely due to absorption from the reaction medium (Supplementary Materials Table S2). Interestingly, the section in contact with the organic phase contained slightly more chlorine (0.99%) compared to the aqueous-phase section (0.54%), though this difference is negligible and not considered significant. However, no peaks containing chlorine are present in the XPS spectra due to its small amount. Overall, these scale-up experiment results illustrate the advantage of photocatalytic panels for scaling up CHA and potentially other oxidation reactions by simply enlarging the size of CN photocatalyst films in CHA-water biphasic systems.

4. Conclusions

In this work, we demonstrated the advantages of CN films as photocatalysts for the selective photo-oxidation of cyclohexane in both monophasic and biphasic systems. In the biphasic system, adding the acidic aqueous phase enhanced the total yield of the products. Furthermore, the type and concentration of the acid in the aqueous phase influenced the selectivity of the products; HCl favours the formation of cyclohexanone, while HBr favours cyclohexanol. Moreover, with the observed excellent recyclability of the CN panels compared to the CN powder, we demonstrated the scale-up concept using 6 × 2 cm²-sized CN panels, which exhibit excellent long-term stability and photocatalytic activity even after 6 days.

Supplementary Materials

The additional data and information can be downloaded at: https://media.sciltp.com/articles/others/25111215 24546058/Photocatalysis-25090043-Supplementary-Materials-FC-done.pdf. Figure S1: Structural and optical characterizations of CN-10, CN-M10, CN-20, and CN-M20 films. (**a**) X-ray diffraction (XRD) patterns; (**b**) Fourier-transform infrared (FTIR) spectra; (**c**) photoluminescence (PL) spectra; (**d**) F(R) spectra and (**e**) Tauc plot analyses. Figure S2: FTIR spectrum of CN-10. Figure S3: (**a**) C 1s; and (**b**) N 1s XPS spectra of the CN-10 film; (**c**) XPS survey spectrum. Table S1: Elemental analysis of the CN-10 as was detected by XPS. Figure S4: UV–vis diffuse reflectance spectra, presented as the Kubelka-Munk function, F(R), of CN-10. Figure S5: PL spectra of the CN films; λ_{ex} = 380 nm. Figure S6: Additional top-view SEM images of CN-10. Figure S7: Multi-photoreactor

light spectrum, irradiation wavelength is 390 nm. Figure S8: Optimization experiments of photocatalytic cyclohexane oxidation conditions. (**a**) Optimization of film; (**b**) Optimization of CN-10 substrate. Figure S9: (**a**) an illustration; and (**b**) a digital picture of the biphasic aqueous-organic system; **(c)** The photocatalytic system, using white LED. The digital pictures were taken from the large-scale system. Figure S10: Reproducibility of the photocatalytic reaction, using CN-10 as the photocatalyst and adding 1 M HCl to the reaction. Figure S11: A comparison of product yield obtained in a biphasic system consisting of CHA with 1 M HBr, 1 M HCl, 1:1 mixture of 0.5 M HBr and 0.5 M HCl, and 1:1 mixture of 1 M HBr and 1 M HCl. Figure S12: A comparison of product yield obtained in four different systems: pure CHA purged with Ar, pure CHA purged with O_2, biphasic system of CHA with 1 M HCl purged with Ar, and biphasic system of CHA with 1 M HCl purged with O_2. Figure S13: Irradiation spectrum of the 100 W, white LED used for the large-scale photocatalytic oxidation reactions. Figure S14: GC-MS curves showing the evolution of the major products in the large scale reactions: cyclohexanol, cyclohexanone and chlorocyclohexane in (**a**) pure CHA and (**b**) CHA + 1 M HCl. Figure S15: KA oil yield vs. time for pure CHA and the biphasic system consisting of CHA + 1 M HCl. Figure S16: (**a**) XRD patterns and (**b**) FTIR spectra of pristine CN-10 film (purple) compared to used CN-film in the aqueous phase (pink) and organic phase (dark cyan) in the biphasic system. Figure S17: SEM imaging of the CN-10 film in (**a**,**c**) aqueous phase (1 M HCl) and (**b**,**d**) organic phase (CHA). Figure S18: (**a**) C 1s and (**b**) N 1s spectra of the CN-10 film before and after the long-term photocatalytic measurements. Table S2. XPS analysis of the CN-10 film elemental composition before and after the long-term photocatalytic reaction.

Author Contributions

A.T. and V.R.B.: wrote the initial draft of the manuscript; A.T.: performed most of the experiments and analyzed the data; V.R.B.: provided scientific guidance and graphics; M.S.: supervised the study, co-wrote and reviewed the paper, and acquired funding. All authors have read and agreed to the published version of the manuscript.

Funding

This project was supported by the Israeli Ministry of Innovation, Science & Technology (collaboration with China), Grant No. 0007247 and by the Israel Council for Higher Education (VATAT) project “A collaborative Center for Advanced Solar Energy Research in Israel”.

Institutional Review Board Statement

Not applicable.

Informed Consent Statement

Not applicable.

Data Availability Statement

The data is available by request.

Acknowledgments

The authors thank Rotem Geva and Keren Barchichat for helping with data analysis, and Natalya Froumin from Ilse Katz Institute for Nanoscale Science and Technology for conducting XPS measurements.

Conflicts of Interest

The authors declare no conflict of interest.

Use of AI and AI-Assisted Technologies

During the preparation of this work, the authors used ChatGPT for proofreading and language refinement; all scientific content was written by the authors. After using this tool, the authors reviewed and edited the content as needed and take full responsibility for the content of the published article.

Appendix A. GC-MS Data Supporting Product Identification

Appendix A.1. CHA, 35 °C, 24 h

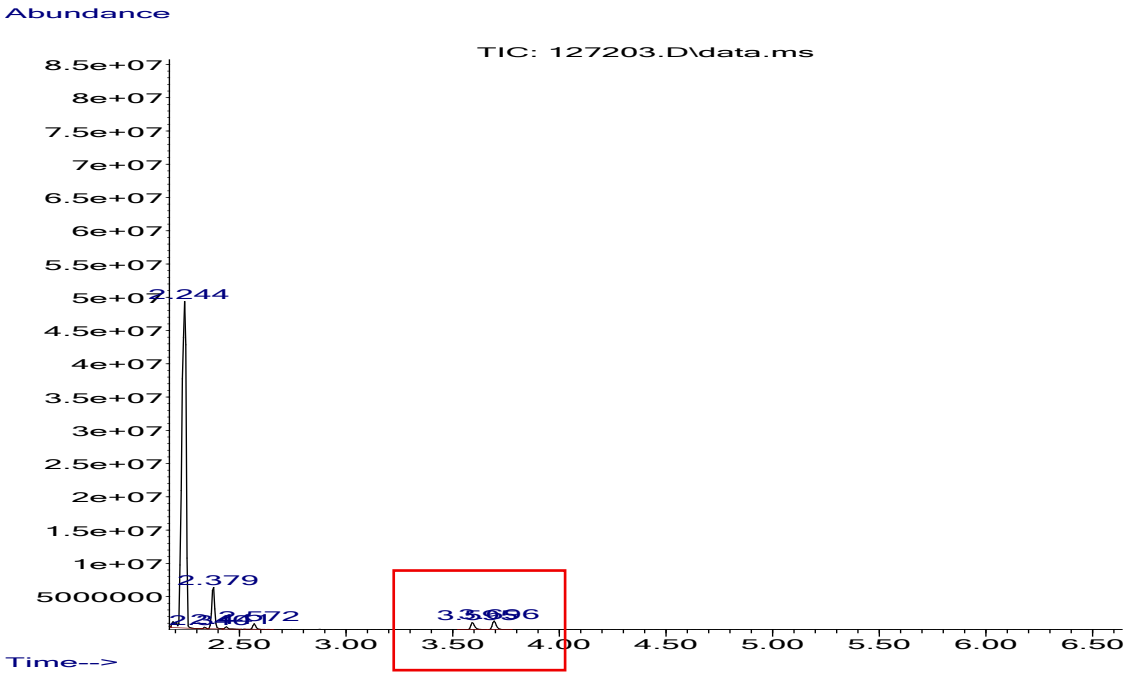

Figure A1. GC chromatogram: CHA, 35 °C, 24 h.

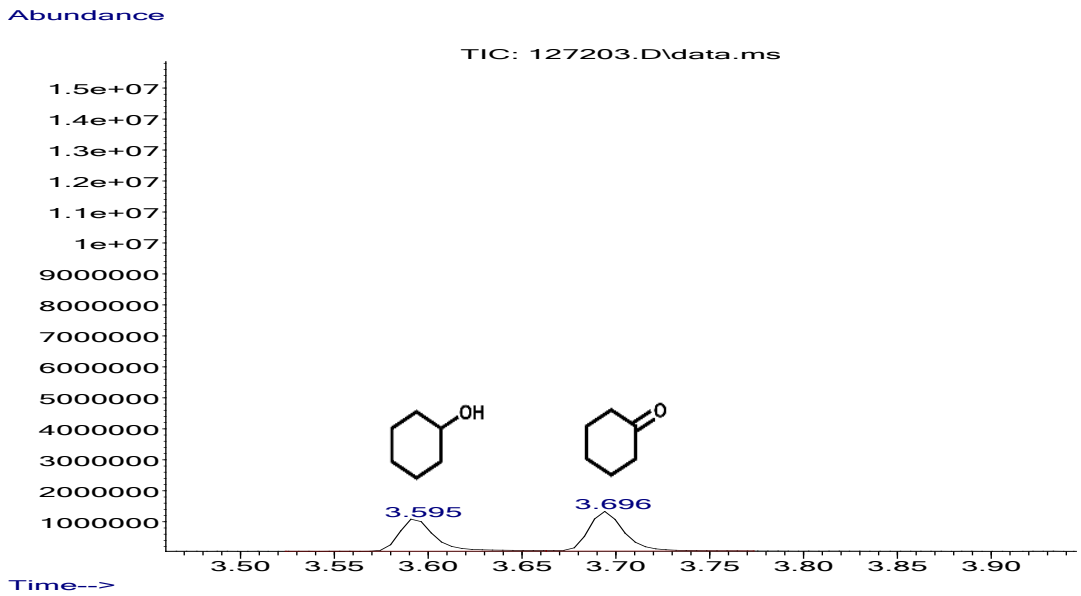

Figure A2. GC chromatogram: CHA, 35 °C, 24 h (zoom in).

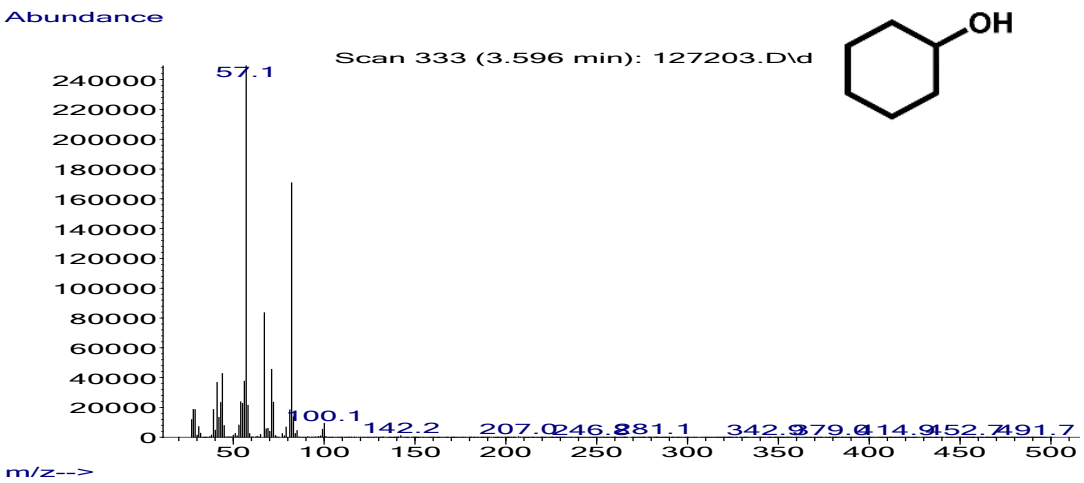

Figure A3. MS spectrum: CHA, 35 °C, 24 h, cyclohexanol.

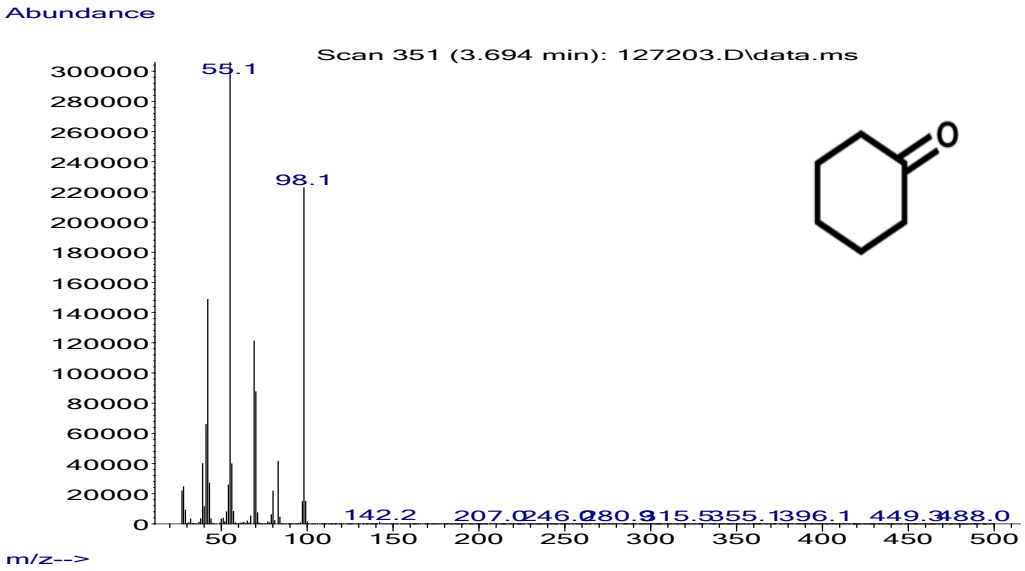

Figure A4. MS spectrum: CHA, 35 °C, 24 h, cyclohexanone.

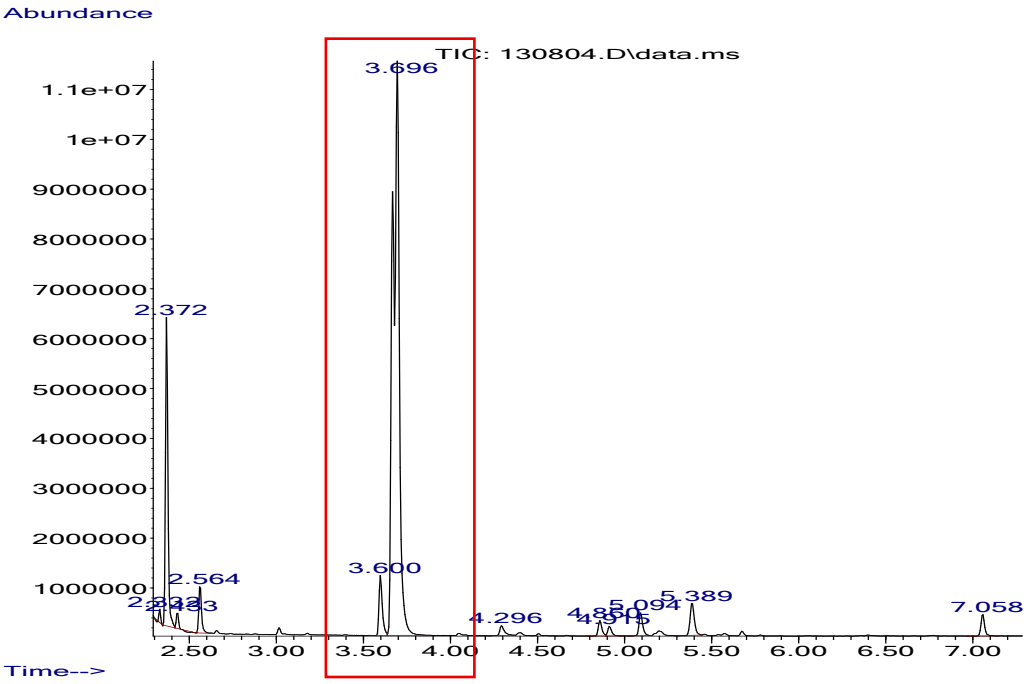

Figure A5. GC chromatogram: CHA + 1 M HCl, 35 °C, 24 h.

Appendix A.2. CHA + 1 M HCl, 35 °C, 24 h

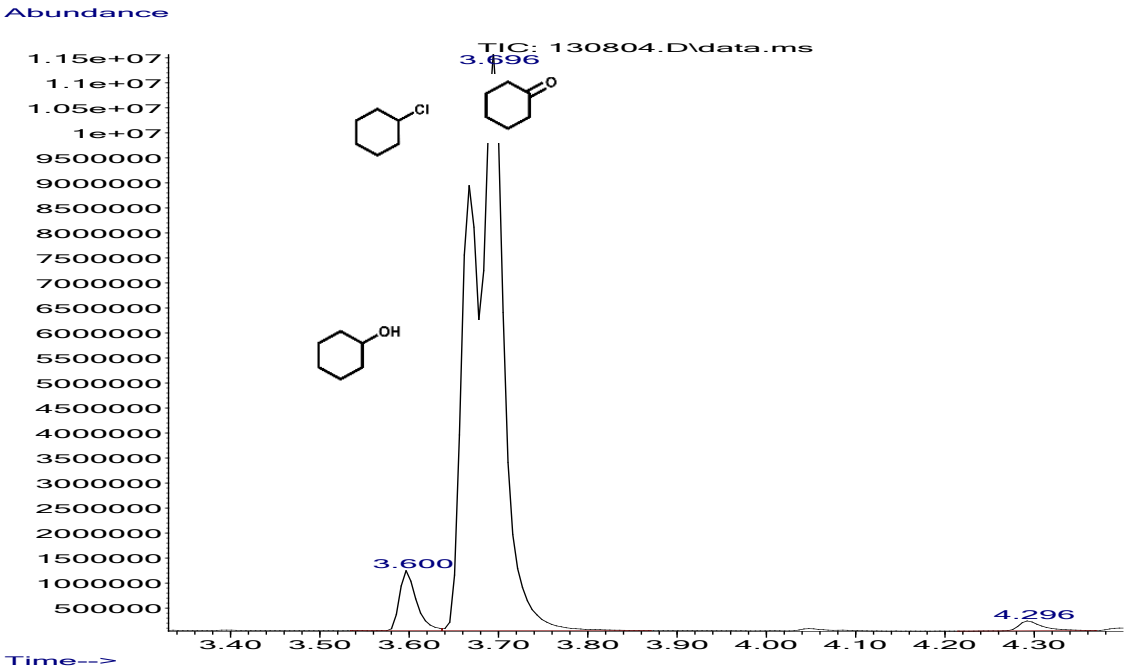

Figure A6. GC chromatogram: CHA + 1 M HCl, 35 °C, 24 h (zoom in).

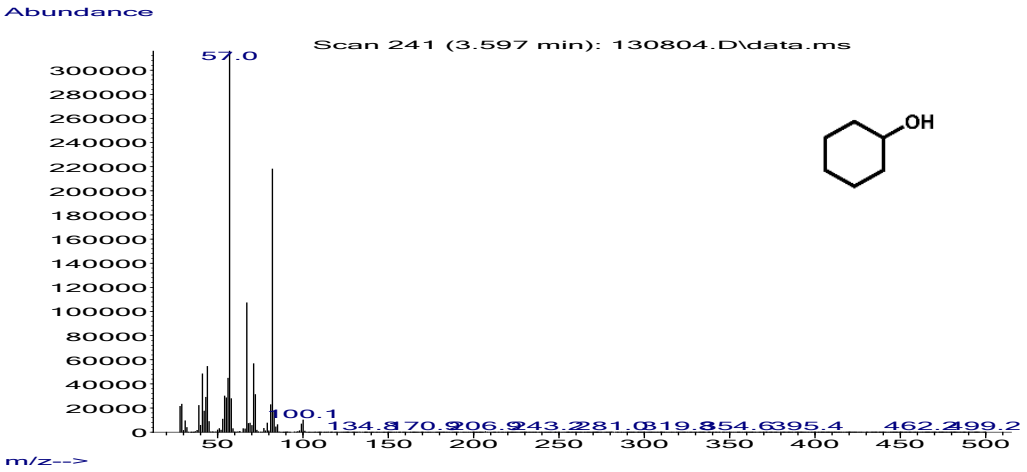

Figure A7. MS spectrum: CHA + 1 M HCl, 35 °C, 24 h, cyclohexanol.

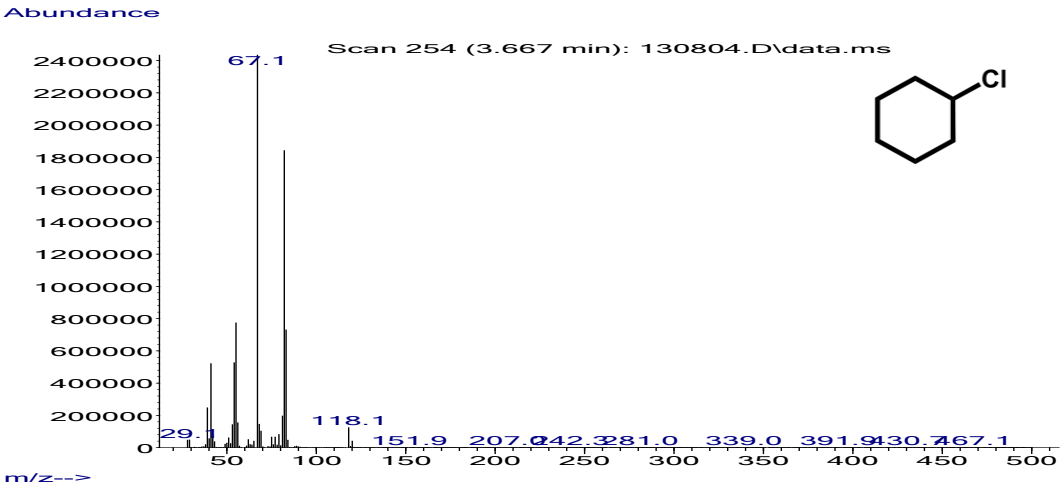

Figure A8. MS spectrum: CHA + 1 M HCl, 35 °C, 24 h, chlorocyclohexane.

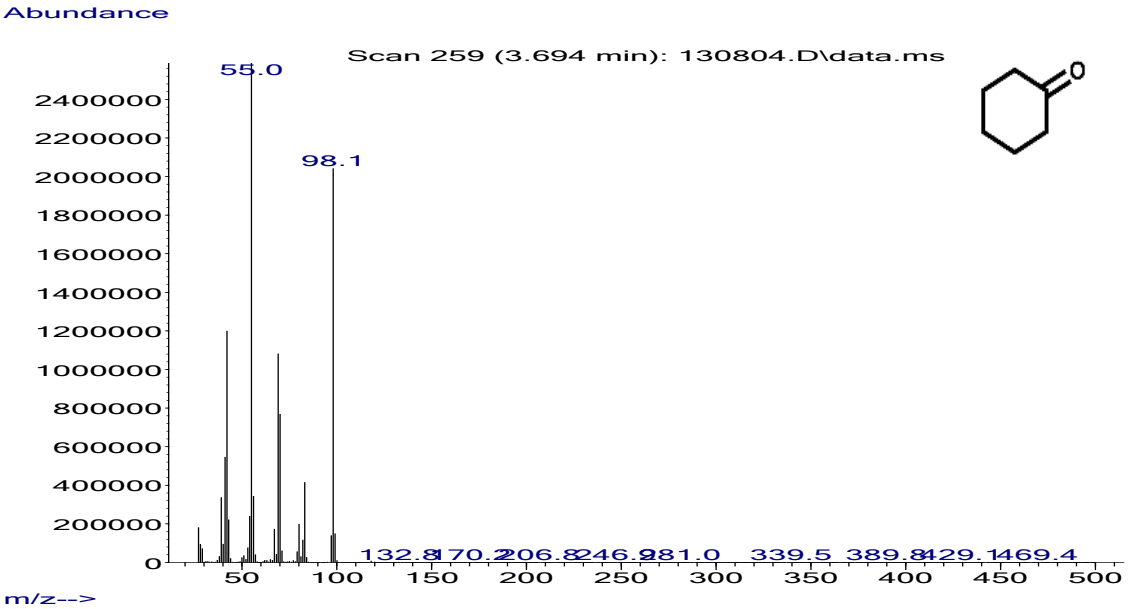

Figure A9. MS spectrum: CHA + 1 M HCl, 35 °C, 24 h, cyclohexanone.

Appendix A.3. CHA + 1 M HBr, 35 °C, 24 h

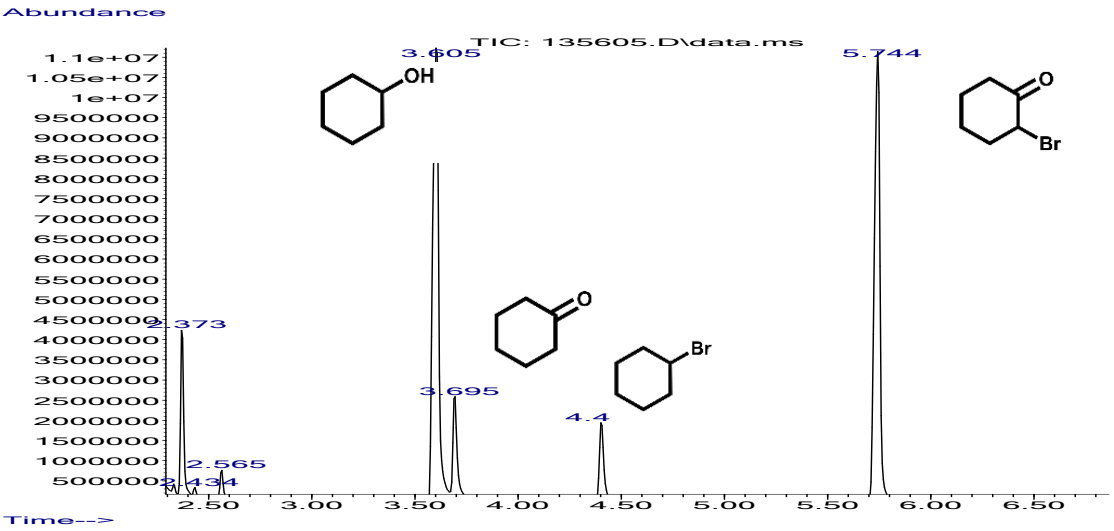

Figure A10. GC chromatogram: CHA + 1 M HBr, 35 °C, 24 h.

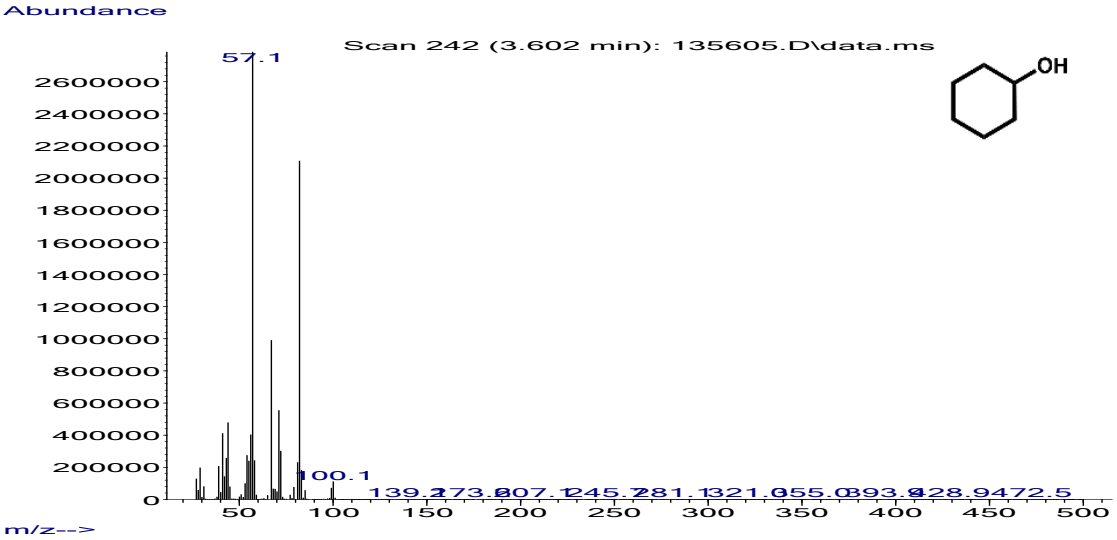

Figure A11. MS spectrum: CHA + 1 M HBr, 35 °C, 24 h, cyclohexanol.

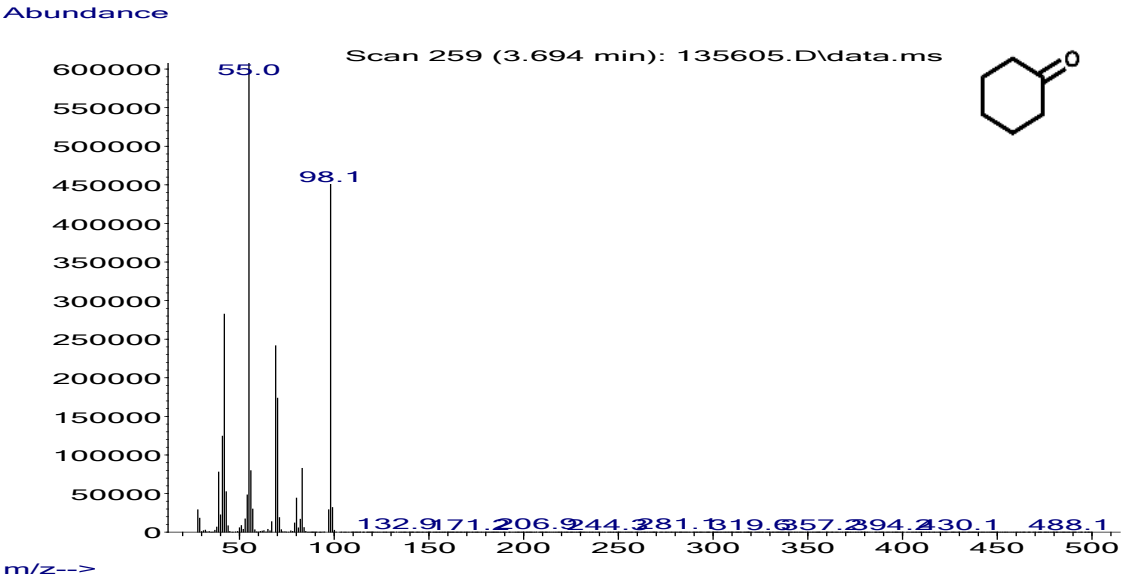

Figure A12. CHA + 1 M HBr, 35 °C, 24 h, cyclohexanone.

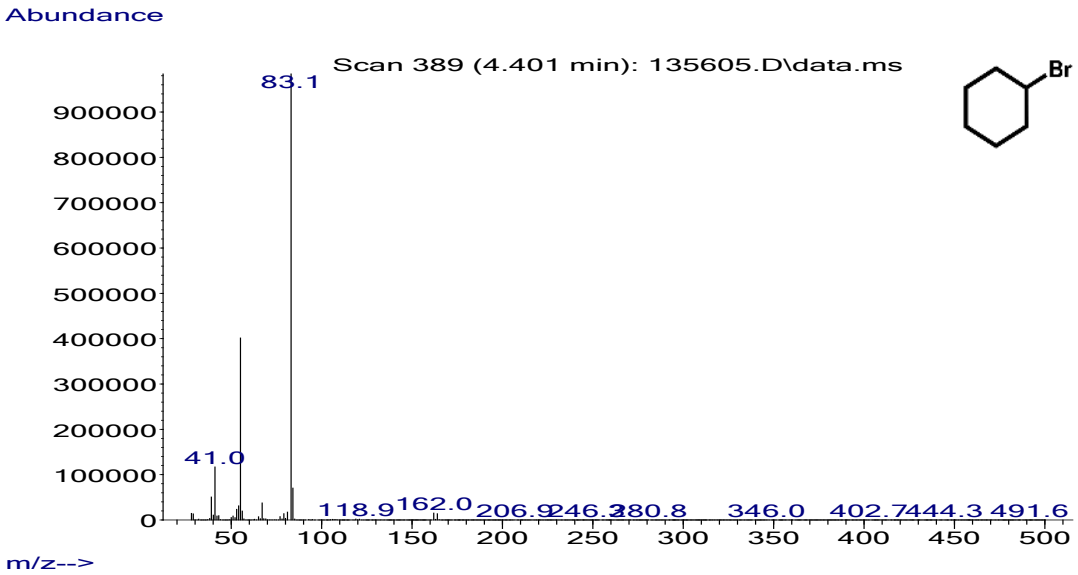

Figure A13. CHA + 1 M HBr, 35 °C, 24 h, bromocyclohexane.

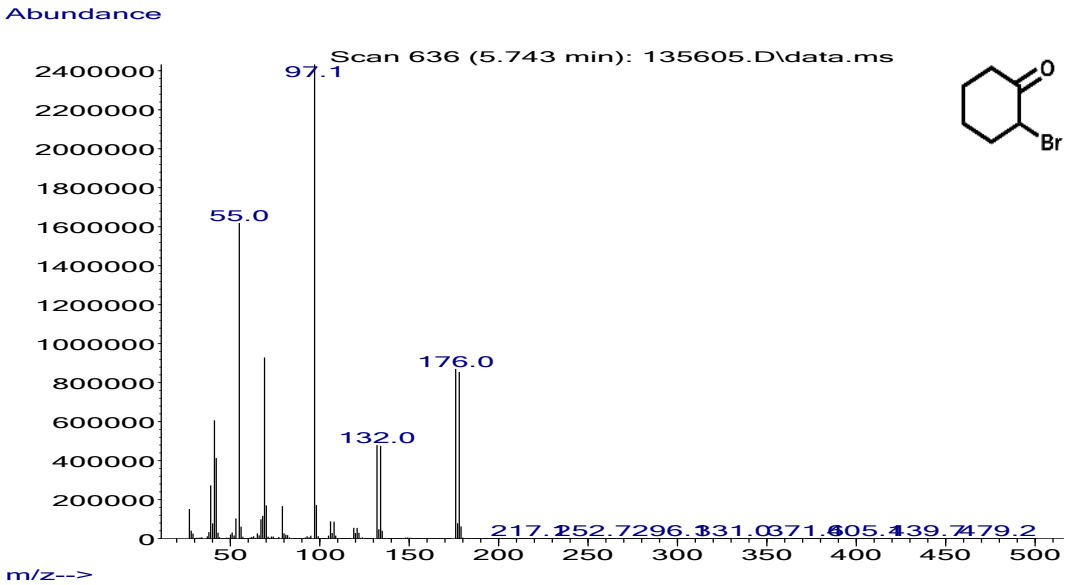

Figure A14. CHA + 1 M HBr, 35 °C, 24 h, 2-bromocyclohexanone.

Appendix A.4. CHA + 1 M HBr + 1 M HCl, 35 °C, 24 h

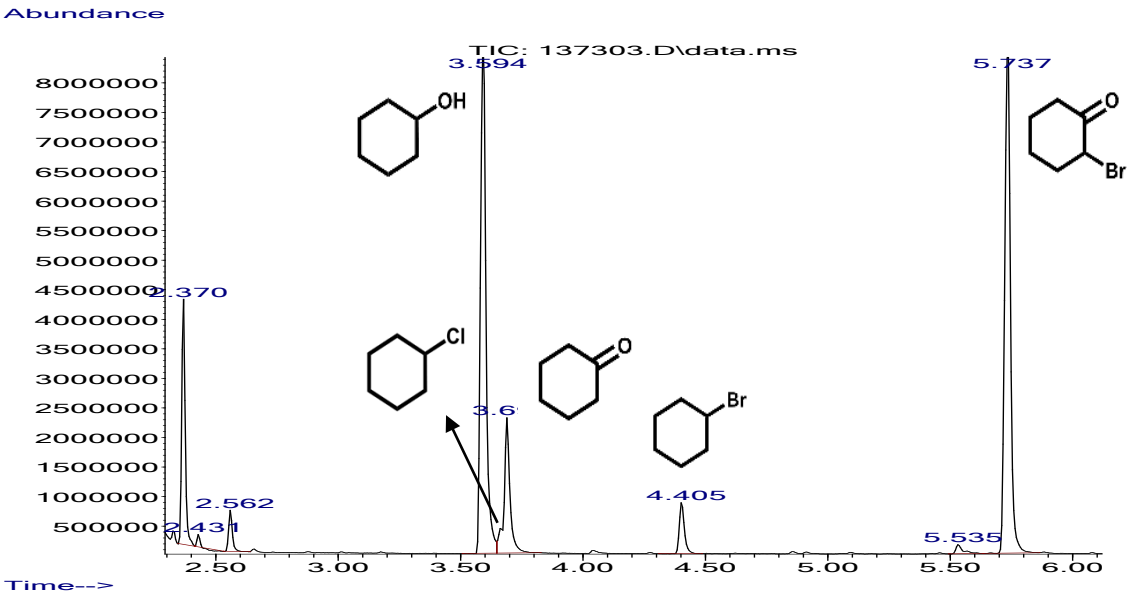

Figure A15. GC chromatogram: CHA + 1 M HBr + 1 M HCl, 35 °C, 24 h.

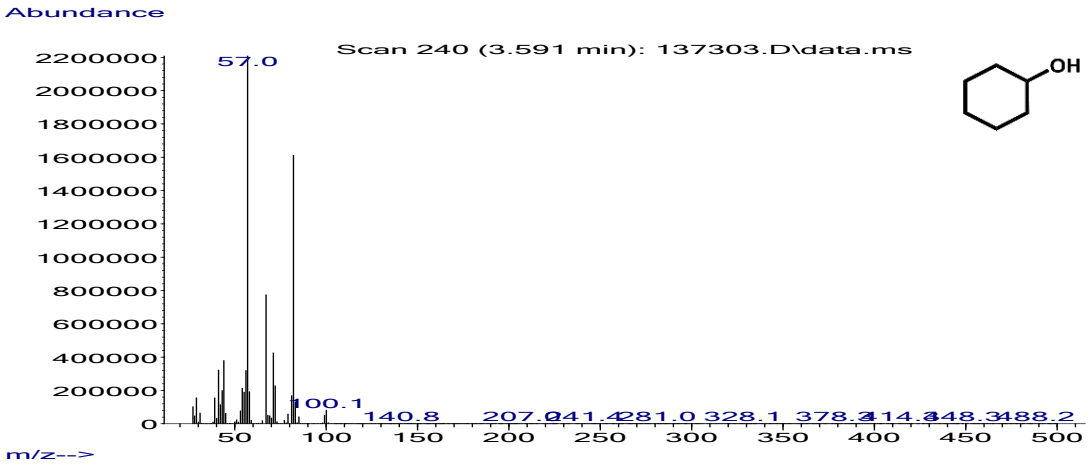

Figure A16. MS spectrum: CHA + 1 M HBr + 1 M HCl, 35 °C, 24 h, cyclohexanol.

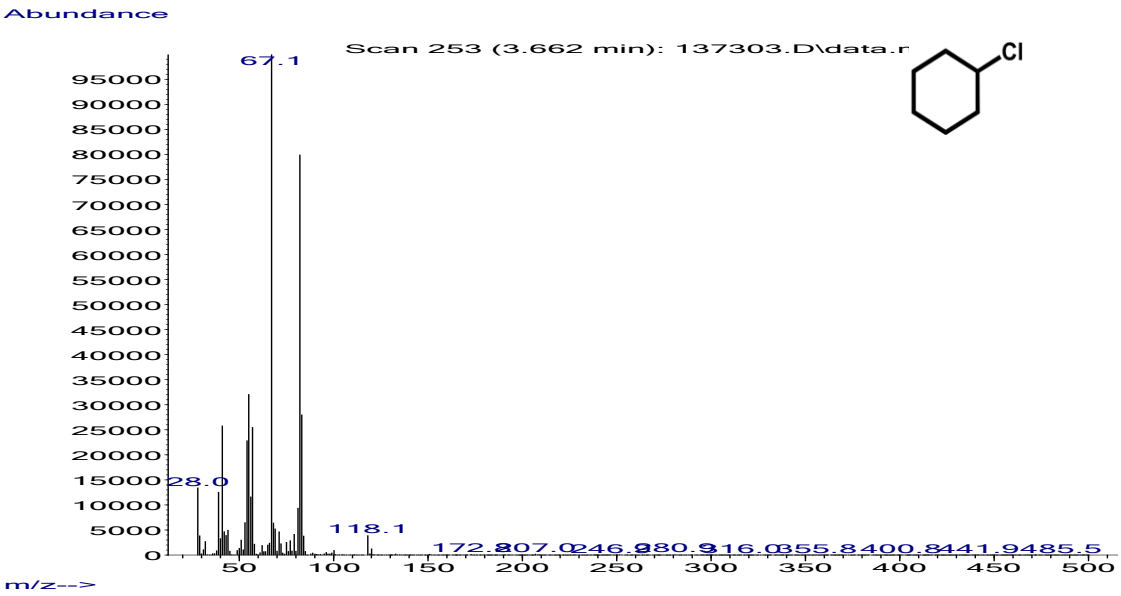

Figure A17. MS spectrum: CHA + 1 M HBr + 1 M HCl, 35 °C, 24 h, chlorocyclohexane.

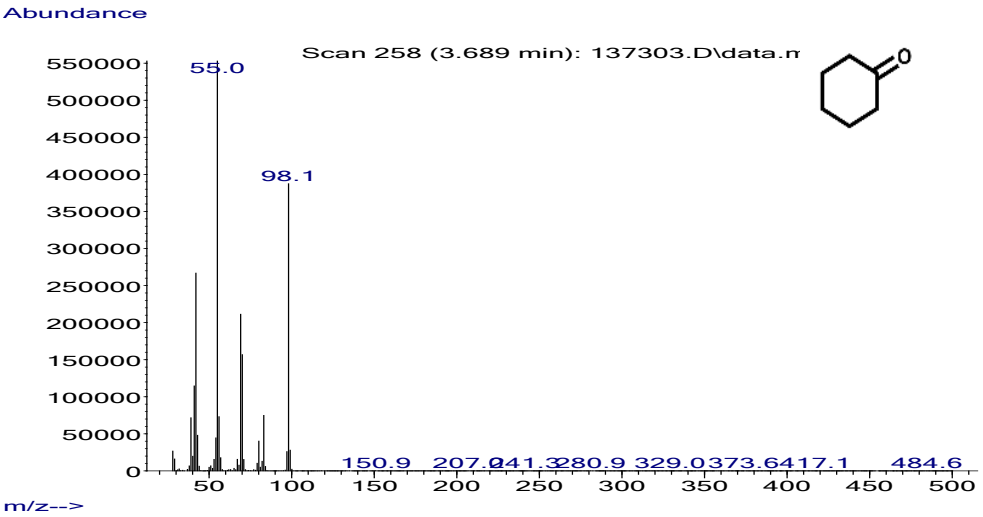

Figure A18. MS spectrum: CHA + 1 M HBr + 1 M HCl, 35 °C, 24 h, cyclohexanone.

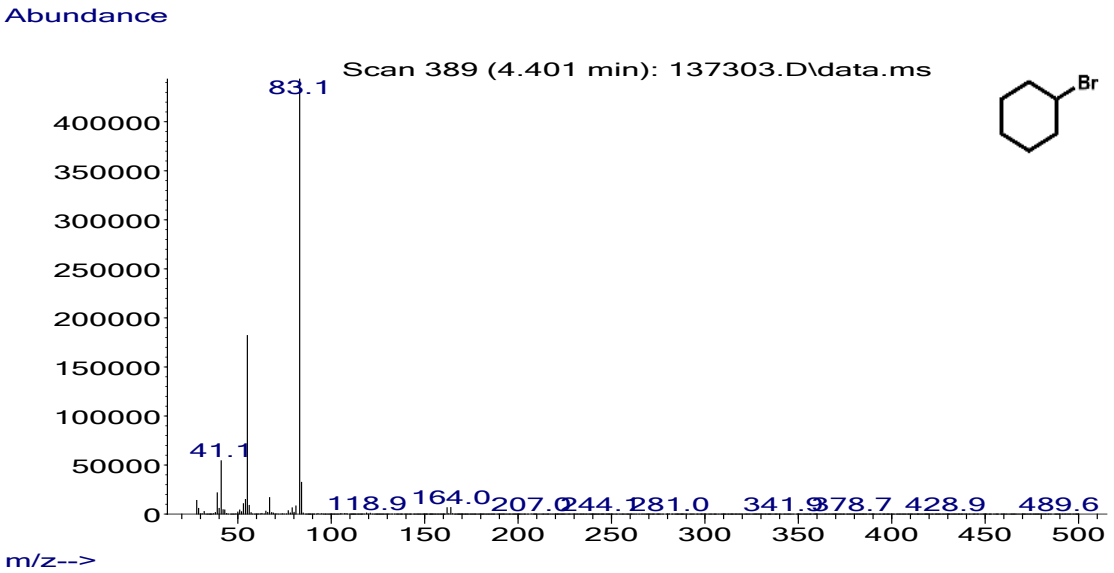

Figure A19. MS spectrum: CHA + 1 M HBr + 1 M HCl, 35 °C, 24 h, bromocyclohexane.

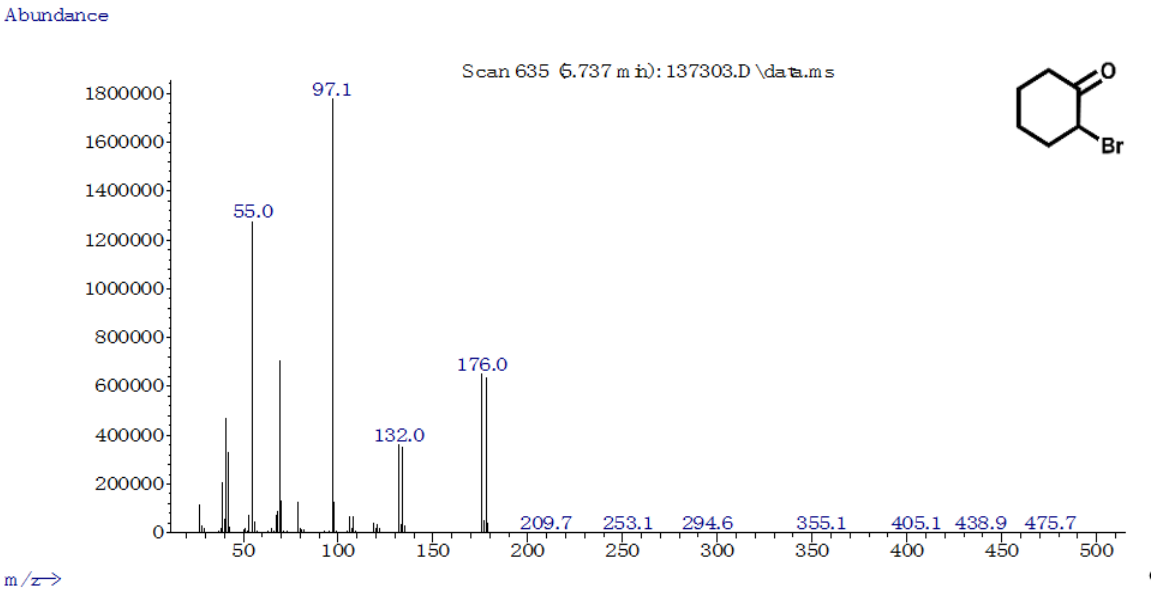

Figure A20. MS spectrum: CHA + 1 M HBr + 1 M HCl, 35 °C, 24 h, 2-bromocyclohexanone.

Appendix A.5. CHA + 2 M HBr + 2 M HCl, 35 °C, 24 h

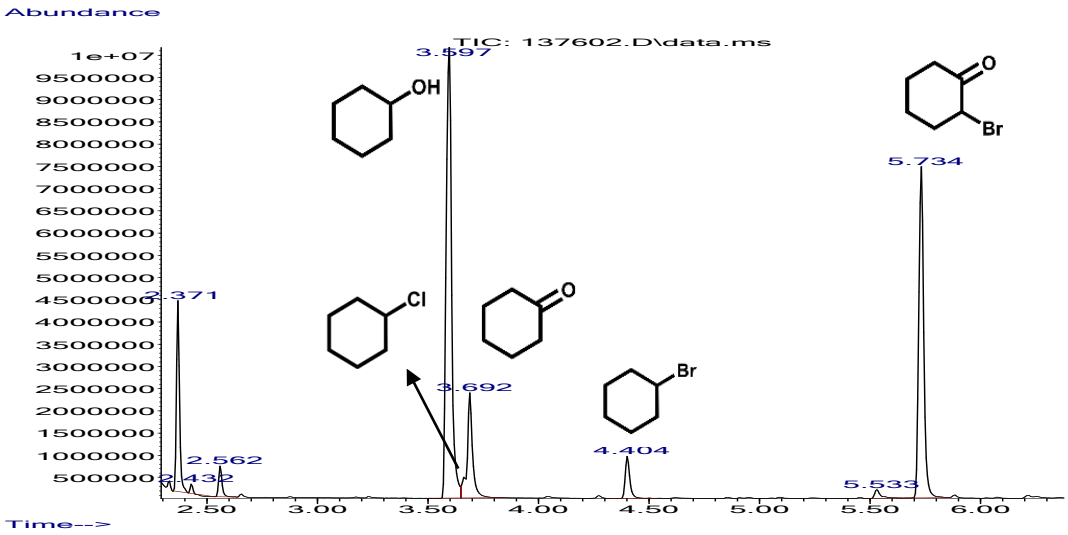

Figure A21. GC chromatogram: CHA + 2 M HBr + 2 M HCl, 35 °C, 24 h.

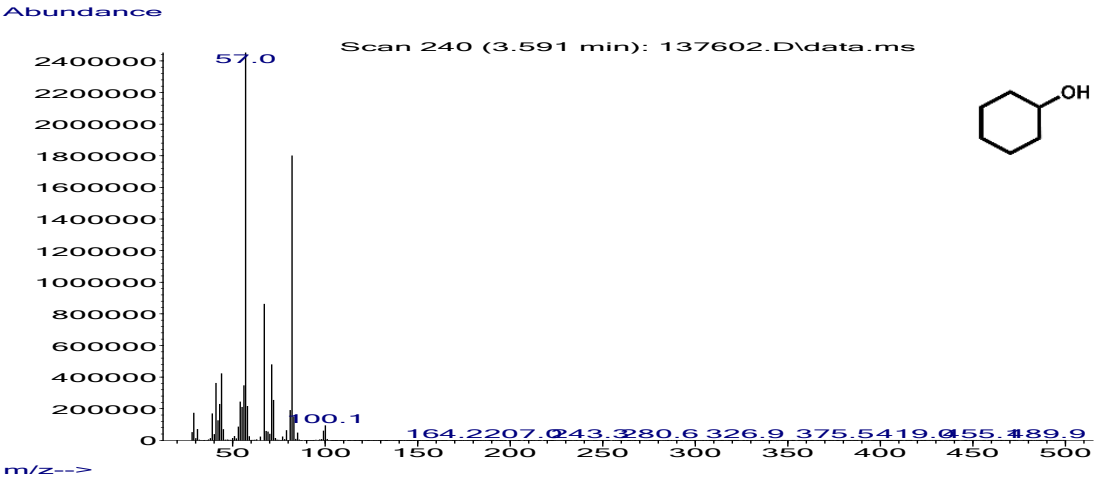

Figure A22. MS spectrum: CHA + 2 M HBr + 2 M HCl, 35 °C, 24 h, cyclohexanol.

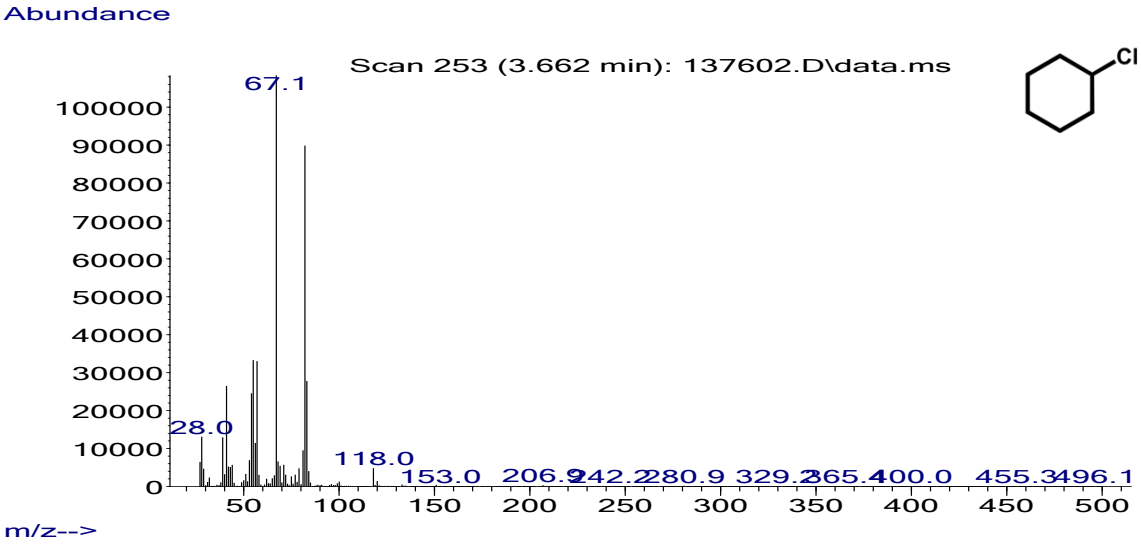

Figure A23. MS spectrum: CHA + 2 M HBr + 2 M HCl, 35 °C, 24 h, chlorocyclohexane.

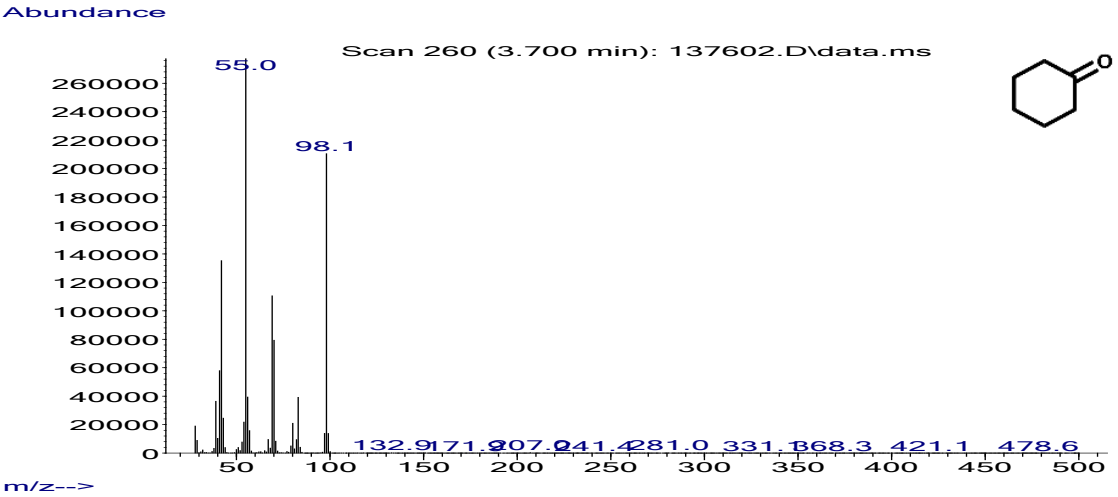

Figure A24. MS spectrum: CHA + 2 M HBr + 2 M HCl, 35 °C, 24 h, cyclohexanone.

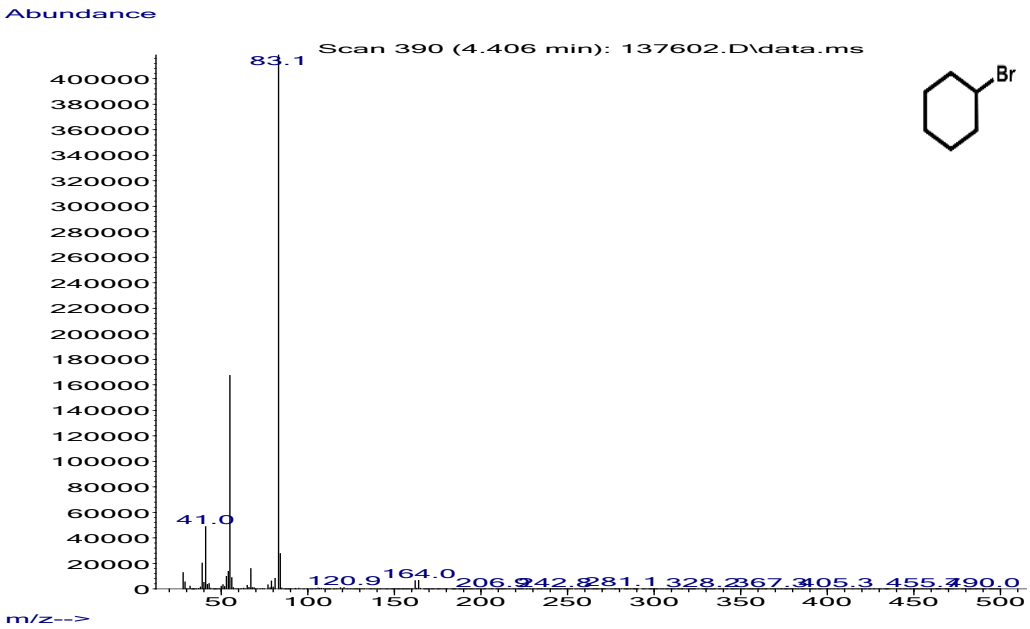

Figure A25. MS spectrum: CHA + 2 M HBr + 2 M HCl, 35 °C, 24 h, bromocyclohexane.

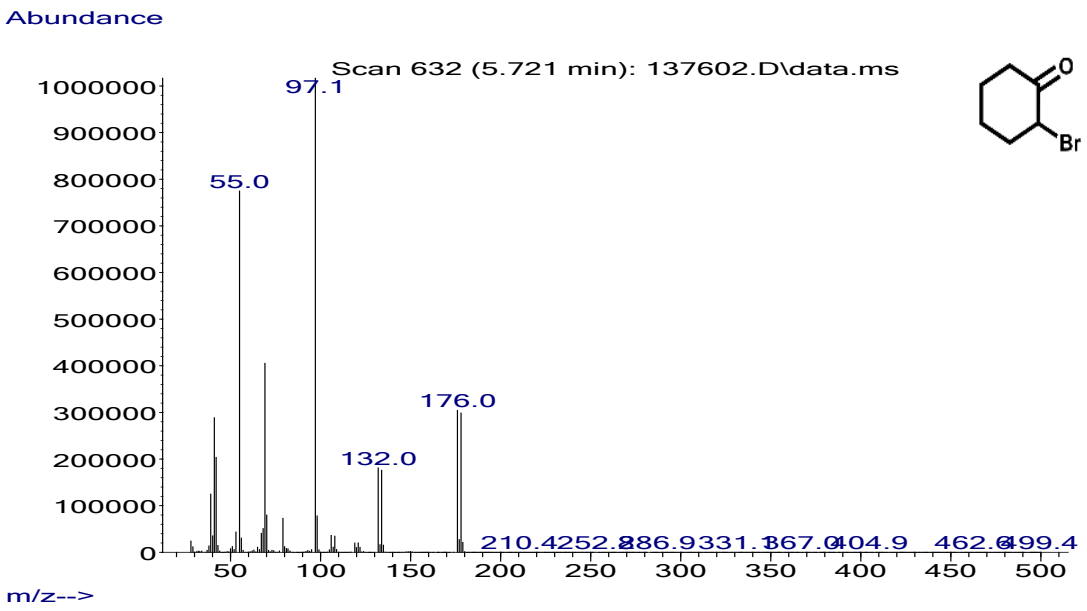

Figure A26. MS spectrum: CHA + 2 M HBr + 2 M HCl, 35 °C, 24 h, 2-bromocyclohexanone.

References

1. Castellan, A.; Bart, J.C.J.; Cavallaro, S. Industrial production and use of adipic acid. *Catal. Today* **1991**, *9*, 237–254. https://doi.org/10.1016/0920-5861(91)80049-F.
2. Huo, H.; Guo, B.; Ma, G.; et al. Recent progress in strategies to enhance the photocatalytic oxidation performance of cyclohexane. *J. Environ. Chem. Eng.* **2024**, *12*, 113504. https://doi.org/10.1016/j.jece.2024.113504.
3. Montjoy, D.G.; Wilson, E.A.K.; Hou, H.; et al. Photocatalytic cyclohexane oxidation and epoxidation using hedgehog particles. *Nat. Commun.* **2023**, *14*, 857. https://doi.org/10.1038/s41467-023-36473-5.
4. Schuchardt, U.; Cardoso, D.; Sercheli, R.; et al. Cyclohexane oxidation continues to be a challenge. *Appl. Catal. A Gen.* **2001**, *211*, 1–17. https://doi.org/10.1016/S0926-860X(01)00472-0.
5. Luo, L.; Zhang, T.; Wang, M.; et al. Recent Advances in Heterogeneous Photo-Driven Oxidation of Organic Molecules by Reactive Oxygen Species. *ChemSusChem* **2020**, *13*, 5173–5184. https://doi.org/10.1002/cssc.202001398.
6. Chen, L.; Tang, J.; Song, L.-N.; et al. Heterogeneous photocatalysis for selective oxidation of alcohols and hydrocarbons. *Appl. Catal. B Environ.* **2019**, *242*, 379–388. https://doi.org/10.1016/j.apcatb.2018.10.025.
7. Wang, H.; Gao, X.; Lv, Z.; et al. Recent Advances in Oxidative R1-H/R2-H Cross-Coupling with Hydrogen Evolution via Photo-/Electrochemistry. *Chem. Rev.* **2019**, *119*, 6769–6787. https://doi.org/10.1021/acs.chemrev.9b00045.
8. Wu, W.; He, X.; Fu, Z.; et al. Metal chlorides-catalyzed selective oxidation of cyclohexane by molecular oxygen under visible light irradiation. *J. Catal.* **2012**, *286*, 6–12. https://doi.org/10.1016/j.jcat.2011.09.034.
9. She, J.; Fu, Z.; Li, J.; et al. Visible light-triggered vanadium-substituted molybdophosphoric acids to catalyze liquid phase oxygenation of cyclohexane to KA oil by nitrous oxide. *Appl. Catal. B Environ.* **2016**, *182*, 392–404. https://doi.org/10.1016/j.apcatb.2015.09.048.
10. Fu, C.; Du, J.; Shi, N.; et al. Strongly active and environmentally friendly WO_3/C_3N_4 photocatalysts for converting cyclohexane to cyclohexanone under ambient conditions. *Sci. Rep.* **2024**, *14*, 17947. https://doi.org/10.1038/s41598-024-68319-5.
11. Zhou, H.; Shao, Y.; Zhou, Z.; et al. Bio-inspired V-TiO_2 architectures with regulable surface ultrastructure for visible-light photocatalytic selective oxidation of cyclohexane. *Appl. Surf. Sci.* **2023**, *622*, 156957. https://doi.org/10.1016/j.apsusc.2023.156957.
12. Xu, G.; Zhang, Y.; Peng, D.; et al. MOF derived carbon modified porous TiO_2 mixed-phase junction with efficient visible-light photocatalysis for cyclohexane oxidation. *Mater. Res. Bull.* **2022**, *146*, 111602. https://doi.org/10.1016/j.materresbull.2021.111602.
13. Teramura, K.; Tanaka, T.; Yamamoto, T.; et al. Photo-oxidation of cyclohexane over alumina-supported vanadium oxide catalyst. *J. Mol. Catal. A: Chem.* **2001**, *165*, 299–301. https://doi.org/10.1016/S1381-1169(00)00417-9.
14. Wang, K.; Xue, B.; Wang, J.-L.; et al. Efficient and selective oxidation of cyclohexane to cyclohexanone over flake hexagonal boron nitride/titanium dioxide hybrid photocatalysts. *Mol. Catal.* **2021**, *505*, 111530. https://doi.org/10.1016/j.mcat.2021.111530.
15. Ichihashi, Y.; Saijo, S.; Taniguchi, M.; et al. Study of Cyclohexane Photooxidation over Pt-WO_3 Catalysts Mixed with TiO_2 under Visible Light Irradiation. *Mater. Sci. Forum* **2010**, *658*, 149–152. https://doi.org/10.4028/www.scientific.net/MSF.658.149.
16. Thomas, A.; Fischer, A.; Goettmann, F.; et al. Graphitic carbon nitride materials: Variation of structure and morphology and their use as metal-free catalysts. *J. Mater. Chem.* **2008**, *18*, 4893–4908. https://doi.org/10.1039/b800274f.
17. Wang, Y.; Wang, X.; Antonietti, M. Polymeric Graphitic Carbon Nitride as a Heterogeneous Organocatalyst: From Photochemistry to Multipurpose Catalysis to Sustainable Chemistry. *Angew. Chem. Int. Ed.* **2012**, *51*, 68–89. https://doi.org/10.1002/anie.201101182.
18. Wang, X.; Maeda, K.; Thomas, A.; et al. A metal-free polymeric photocatalyst for hydrogen production from water under visible light. *Nat. Mater.* **2009**, *8*, 76–80. https://doi.org/10.1038/nmat2317.
19. Wang, X.; Blechert, S.; Antonietti, M. Polymeric Graphitic Carbon Nitride for Heterogeneous Photocatalysis. *ACS Catal.* **2012**, *2*, 1596–1606. https://doi.org/10.1021/cs300240x.
20. Wang, X.; Maeda, K.; Chen, X.; et al. Polymer Semiconductors for Artificial Photosynthesis: Hydrogen Evolution by Mesoporous Graphitic Carbon Nitride with Visible Light. *J. Am. Chem. Soc.* **2009**, *131*, 1680–1681. https://doi.org/10.1021/ja809307s.
21. Maeda, K.; Wang, X.; Nishihara, Y.; et al. Photocatalytic Activities of Graphitic Carbon Nitride Powder for Water Reduction and Oxidation under Visible Light. *J. Phys. Chem. C* **2009**, *113*, 4940–4947. https://doi.org/10.1021/jp809119m.
22. Wang, J.; Yang, J.; Zeng, S.; et al. Efficient photocatalytic oxidation of cyclohexane to KA oil by carbon nitride hybridized decatungstate under visible light. *J. Catal.* **2025**, *443*, 115996. https://doi.org/10.1016/j.jcat.2025.115996.
23. Xu, M.; Yu, Y.; Shi, G.; et al. Curved Surface of Graphitic Carbon Nitride Boosting Cyclohexane Oxidation over Single-Atom Catalysts. *ACS Appl. Nano Mater.* **2024**, *7*, 11952–11964. https://doi.org/10.1021/acsanm.4c01538.

24. Dam, B.; Das, B.; Patel, B.K. Graphitic carbon nitride materials in dual metallo-photocatalysis: A promising concept in organic synthesis. *Green Chem.* **2023**, *25*, 3374–3397. https://doi.org/10.1039/D3GC00669G.
25. Zhou, P.; Cai, Y.; Tang, Y. Recent advances on carbon nitride-based photocatalysts for organic transformations in aqueous media. *Org. Chem. Front.* **2024**, *11*, 4624–4638. https://doi.org/10.1039/D4QO00955J.
26. Savateev, A.; Antonietti, M. Heterogeneous Organocatalysis for Photoredox Chemistry. *ACS Catal.* **2018**, *8*, 9790–9808. https://doi.org/10.1021/acscatal.8b02595.
27. Verma, S.K.; Verma, R.; Girish, Y.R.; et al. Heterogeneous graphitic carbon nitrides in visible-light-initiated organic transformations. *Green Chem.* **2022**, *24*, 438–479. https://doi.org/10.1039/D1GC03490A.
28. Tashakory, A.; Mondal, S.; Battula, V.R.; et al. Minute-Scale High-Temperature Synthesis of Polymeric Carbon Nitride Photoanodes. *Small Struct.* **2024**, *5*, 2400123. https://doi.org/10.1002/sstr.202400123.
29. Zhao, C.; Li, Q.; Xie, Y.; et al. Three-dimensional assemblies of carbon nitride tubes as nanoreactors for enhanced photocatalytic hydrogen production. *J. Mater. Chem. A* **2020**, *8*, 305–312. https://doi.org/10.1039/C9TA10688J.
30. Fan, J.-M.; Chen, J.-J.; Zhang, Q.; et al. An Amorphous Carbon Nitride Composite Derived from ZIF-8 as Anode Material for Sodium-Ion Batteries. *ChemSusChem* **2015**, *8*, 1856–1861. https://doi.org/10.1002/cssc.201500192.
31. Ech-chamikh, E.; Essafti, A.; Ijdiyaou, Y.; et al. XPS study of amorphous carbon nitride (a-C:N) thin films deposited by reactive RF sputtering. *Sol. Energy Mater. Sol. Cells* **2006**, *90*, 1420–1423. https://doi.org/10.1016/j.solmat.2005.10.007.
32. Alwin, E.; Nowicki, W.; Wojcieszak, R.; et al. Elucidating the structure of the graphitic carbon nitride nanomaterials via X-ray photoelectron spectroscopy and X-ray powder diffraction techniques. *Dalton Trans.* **2020**, *49*, 12805–12813. https://doi.org/10.1039/D0DT02325F.
33. Mondal, S.; Mark, G.; Tashakory, A.; et al. Porous carbon nitride rods as an efficient photoanode for water splitting and benzylamine oxidation. *J. Mater. Chem. A* **2024**, *12*, 11502–11510. https://doi.org/10.1039/D4TA00237G.
34. Mai, J.; Fang, Y.; Liu, J.; et al. Simple synthesis of WO_3-Au composite and their improved photothermal synergistic catalytic performance for cyclohexane oxidation. *Mol. Catal.* **2019**, *473*, 110389. https://doi.org/10.1016/j.mcat.2019.04.018.
35. Wang, K.; Wang, D.; Zhang, X.-Y.; et al. Modular calcination strategy to construct defect-rich nitrogen-doped Nb_2O_5 for boosting photocatalytic oxidation of cyclohexane to cyclohexanone in solvent-free conditions. *Appl. Surf. Sci.* **2023**, *617*, 156600. https://doi.org/10.1016/j.apsusc.2023.156600.
36. Laudadio, G.; Govaerts, S.; Wang, Y.; et al. Selective C(sp^3)−H Aerobic Oxidation Enabled by Decatungstate Photocatalysis in Flow. Angew. *Chem. Int. Ed.* **2018**, *57*, 4078–4082. https://doi.org/10.1002/anie.201800818.
37. Tang, S.; She, J.; Fu, Z.; et al. Study on the formation of photoactive species in $XPMo_{12-n}V_nO_{40}$− HCl system and its effect on photocatalysis oxidation of cyclohexane by dioxygens under visible light irradiation. *Appl. Catal. B Environ.* **2017**, *214*, 89–99. https://doi.org/10.1016/j.apcatb.2017.05.027.
38. Wan, Y.; Guo, Q.; Wang, K.; et al. Efficient and selective photocatalytic oxidation of cyclohexane using O_2 as oxidant in $VOCl_2$ solution and mechanism insight. *Chem. Eng. Sci.* **2019**, *203*, 163–172. https://doi.org/10.1016/j.ces.2019.03.079.
39. Xiang, L.; Fan, J.; Zhong, W.; et al. Heteroatom-induced band-reconstruction of metal vanadates for photocatalytic cyclohexane oxidation towards KA-oil selectivity. *Appl. Catal. A Gen.* **2019**, *575*, 120–131. https://doi.org/10.1016/j.apcata.2019.02.015.
40. Grando, G.; Sportelli, G.; Castellani, G.; et al. Toward Reliable and Reproducible Research in Organic Photocatalysis by Carbon Nitride. *ACS Catal.* **2025**, *15*, 16792–16809. https://doi.org/10.1021/acscatal.5c04794.
41. Li, Z.; Luo, L.; Li, M.; et al. Photoelectrocatalytic C–H halogenation over an oxygen vacancy-rich TiO_2 photoanode. *Nat. Commun.* **2021**, *12*, 6698. https://doi.org/10.1038/s41467-021-26997-z.
42. Saxena, B.; Patel, R.I.; Sharma, A. Visible light-induced bromine radical enhanced hydrogen atom transfer (HAT) reactions in organic synthesis. *RSC Sustain.* **2024**, *2*, 2169–2189. https://doi.org/10.1039/D4SU00214H.
43. Ludwig, C.T.; Owolabi, I.A.; Evans, L.W.; et al. Wavelength-Selective Reactivity of Iron(III) Halide Salts in Photocatalytic C–H Functionalization. *J. Org. Chem.* **2025**, *90*, 3404–3411. https://doi.org/10.1021/acs.joc.4c03107.
44. Bonciolini, S.; Noël, T.; Capaldo, L. Synthetic Applications of Photocatalyzed Halogen-Radical Mediated Hydrogen Atom Transfer for C−H Bond Functionalization. *Eur. J. Org. Chem.* **2022**, *2022*, e202200417. https://doi.org/10.1002/ejoc.202200417.